Solar photospheric network properties and their cycle variation

K. Thibault[1], P. Charbonneau[1] and M. Béland[1,2]

Département de Physique, Université de Montréal

Calcul Québec

kim@astro.umontreal.ca-a

paulchar@astro.umontreal.ca-b

michel.beland@calculquebec.ca-c

Received _____; accepted _____

[1]2900 Édouard-Montpetit, Montréal, Québec, Canada H3T 1J4

[2]2900 Édouard-Montpetit, Montréal, Québec, Canada H3T 1J4

ABSTRACT

We present a numerical simulation of the formation and evolution of the solar photospheric magnetic network over a full solar cycle. The model exhibits realistic behavior inasmuch as it produces large, unipolar concentrations of flux in the polar caps, a power-law flux distribution with index -1.69, a flux replacement timescale of 19.3 h, and supergranule diameters of 20 Mm. The polar behavior is especially telling of model accuracy, as it results from lower-latitude activity, and accumulates the residues of any potential modeling inaccuracy and oversimplification. In this case, the main oversimplification is the absence of a polar sink for the flux, causing an amount of polar cap unsigned flux larger than expected by almost one order of magnitude. Nonetheless, our simulated polar caps carry the proper signed flux and dipole moment, and also show a spatial distribution of flux in good qualitative agreement with recent high-latitude magnetographic observations by Hinode. After the last cycle emergence, the simulation is extended until the network has recovered its quiet Sun initial condition. This permits an estimate of the network relaxation time towards the baseline state characterizing extended periods of suppressed activity, such as the Maunder Grand Minimum. Our simulation results indicate a network relaxation time of 2.9 yr, setting at October 2011 at the soonest the time after which the last solar activity minimum could have qualified as a Maunder-type Minimum. This suggests that photospheric magnetism did not reach its baseline state during the recent extended minimum between cycles 23 and 24.

Subject headings: Sun: surface magnetism, photosphere, activity

1. Introduction

The Sun, like all stars, is magnetic. Its observed photospheric magnetism covers several scales in flux, from sunspots reaching 10^{23} Mx, to faculae, ephemeral regions, the network, all the way down to the inter-network (10^{16-17} Mx), at the resolution limit of current observations (see de Wijn et al. 2009, and references therein). These scales reflect in part the emergence from subphotospheric layers, but they are also coupled by flux reprocessing caused by surface flows: small flux concentrations aggregate, sunspots and large flux concentrations fragment and decay, releasing magnetic flux in the photosphere, contributing to the buildup of faculae and active network (Martin 1988, Schrijver et al. 1997, Simon et al. 2001, Krijger & Roudier 2003).

The photospheric magnetic network is made up of a disjoint assemblage of magnetic flux concentrations, found predominantly at the vertices of adjacent supergranular cells. It represents one of the smallest magnetic flux and length scales currently resolvable on the Sun. Its baseline emissivity contributes to the total solar irradiance (TSI) even in the absence of active regions. It plays a significant role in determining the solar total and spectral irradiance, and, in particular, represents a crucial contribution during extended periods of suppressed magnetic activity, such as the seventeenth century Maunder Minimum, or the recent extended low-activity epoch having preceded the onset of cycle 24.

Because of the wide range of scales involved between the largest active regions (50 Mm and 10^{23} Mx (Foukal 2004, p. 234)) and the network elements (1-10 Mm and 10^{18-19} Mx (Martin et al. 1988; de Wijn 2009)), global simulations of the solar magnetic activity cycle have seldom taken the network explicitly into account (Wang, Nash & Sheeley 1989a, 1989b, Schrijver et al. 2002), or have treated it only statistically as a population (Schrijver et al. 1997, Schrijver 2001). Consequently, the interaction of individual network elements

with one another and between network elements and other larger magnetic structures has so far been left out of full-sphere photospheric flux evolution models. On the other hand, such interactions have been treated in local models "resolving" only a small portion of the solar surface. (Parnell 2001, Simon et al. 2001, Rast 2003, Crouch et al. 2007, Cranmer & van Ballegooijen 2010, Meyer et al. 2011). These processes are highly non-linear, with smaller structures aggregating to form larger ones, and larger structures disintegrating into smaller ones, making models complex and computationally demanding.

The interactions of network elements are driven by the small-scale surface flows (granulation, supergranulation) which displaces elements, leading to surface processes of emergence, coalescence, cancellation, fragmentation, and submergence, and local amplification/regeneration by fast dynamo action. Properties of the magnetic network are thus influenced by the surface flows via the surface interactions.

The magnetic network can be physically characterized through properties such as its distributions of magnetic flux, filling factor, distance between network elements, etc. How these properties vary over the solar activity cycle has remained difficult to establish observationally, with many studies yielding contradictory results. What is now established beyond doubt is that the situation is far more complex than simple in-phase variations. The network's filling factor does vary in phase with the activity cycle, increasing by almost a factor of four between minimum and maximum (Hagenaar et al. 2003). The flux distribution of the magnetic concentrations, including the network elements, is found to be constant by Parnell et al. (2009), while Hagenaar et al. (2003) find that the distribution of larger fluxes varies in phase with the activity cycle, and that only magnetic elements with flux $\leq 10^{19}$ Mx retain a constant distribution. The supergranular size, which sets the spatial scale of the network, increases with solar activity according to McIntosh et al. (2011),

while Meunier et al. (2008) find a decrease in size. Photospheric unsigned magnetic flux varies with the activity cycle (Wang et al. 2005), and so does hemispheric signed flux, with opposite magnetic polarities dominating in opposite hemispheres. The dominant polarity of an hemisphere is the same as the trailing polarity in that hemisphere's active regions, in agreement with Hale's law. Globally, the opposite polarities just about cancel out so that net polarity remains close to zero, as expected from the solenoidal constraint $\nabla \cdot \mathbf{B} = 0$ applied to the complete solar surface.

Latitudinal variations of the network's properties are still little known. While the magnetic filling factor varies in time, Ishikawa et al. (2010) found that at a given phase of the cycle it remains the same at all latitudes (Ishikawa et al. 2010). According to Rimmele & Schroter (1989), smaller supergranules are found around active latitudes, so that the spatial dependence is also time-dependent, due to the drift of active regions from mid-latitudes to the equator as the cycle progresses. Some ranges of flux are found to be typically correlated with active regions and show a similar butterfly diagram, and other flux ranges are found to be anticorrelated, and show a very different butterfly diagram (Jin & Wang 2012). The magnetic network's general behavior thus seems related to the solar activity cycle, although it remains uncertain whether it is the baseline network that varies, or the part of the network fed by the disintegration of active regions, or both.

Observationally, the decomposition of the network into cyclic component and baseline level is difficult, complicating the modelling of the network's contribution to solar activity and TSI, even though the correlation between changes in network coverage and changes in the solar irradiance is well established (Foukal & Lean 1988). Recent findings show that the network's contribution to TSI per unit area strays from linearity at low activity levels, increasing by a factor of 2-4 compared with active region faculae (Foukal

et al. 2011). Low activity levels are of particular interest because they are the ones for which the reconstructed TSI departs from the solar activity indices used in long-term reconstructions (Tapping et al. 2007, Tapping & Valdes 2011).

The level and nature of solar activity in the absence of sunspots and active regions is also uncertain. There is evidence that absence of sunspots does not mean cessation of solar activity: solar eruptions and the interplanetary magnetic field strength both show a cyclic pattern with a period similar to sunspots, and modulate the production of cosmogenic isotopes such as ^{10}Be; the time series for ^{10}Be shows uninterrupted cyclic activity during the Maunder minimum (Beer 2000). The physical nature of this residual cyclic activity remains unknown. The recent 2007-2009 extended minimum in solar activity raised several questions, notably: how long does it take the Sun to return to its baseline activity level after the end of active region emergence, such as seen during long minima? Based on the overall constancy of activity measurements observed in 2009 throughout the unusually long minimum between cycles 23 and 24, during which sunspots all but failed to emerge for nearly 21 months, Schrijver et al. (2011) suggested that the Sun had reached its baseline state, similar to its condition during the Maunder Minimum.

An evolutionary model for the network, covering up to global spatial scales and activity cycle, can provide useful insights towards this question. In this paper we present one such model, and its application to sunspot cycle 21 (1976–1986), a cycle for which detailed information is available regarding the location, flux and magnetic polarity of emerging sunspots and active regions. This surface flux evolution model, described in Crouch et al. (2007) and Thibault et al. (2012; hereafter Paper I), captures the interaction of photospheric network elements as a diffusion-limited aggregation process, subjected to photospheric flux input by emergence and decay of active regions. An overview of the

model is presented in §2 herein. In Paper I we showed that it successfully reproduces the observed power-law form and logarithmic index of the network flux distribution. We could also show that the form of this distribution is rapidly established through surface processes, so that "memory" of the injection scale is rapidly erased. However, by performing distinct simulations with or without injection of active regions, we could also show that the value of the power-law index for the flux distribution is influenced by the presence or absence of active region injection, going from -1.69 in the former case, up to -2.10 in the latter. This indicates that network properties are indeed influenced by the activity cycles, and motivates the present study, which spans a full solar cycle in order to examine in detail the dependence of network properties on latitude and phase of the global activity cycle (§3). We then focus in §4 on the properties and evolution of the polar cap magnetic flux, as a key test on the degree of realism (or lack thereof) of our simulation extended over a solar cycle timescale. We then extend our simulation in §5 with the goal of estimating the relaxation time of the network, i.e., the time required for the network properties to return to their baseline level following the end of active regions emergence at the end of an activity cycle.

2. The network model

Our surface magnetic flux evolution model is described in detail in Crouch et al. (2007) and Paper I; what follows is an overview of its most salient aspects. The model is a Monte Carlo process of diffusion-limited aggregation (DLA) on a spherical surface, where the basic dynamical unit consists of elementary magnetic flux tubes, each assumed to carry the same flux of 10^{17} Mx, consistent with current high resolution magnetographic observations. The latter have a resolution limit in the range 10^{16}—10^{17} Mx (de Wijn et al. 2009). Individual tubes, and clusters thereof, undergo a random walk under the influence of the granular flow. The basic step length and time interval of the random walk is set here at 1.7 Mm and

30 min, somewhat larger than granular scales, in order to permit cycle-length simulations in a reasonable amount of computing time (see Paper I). Tubes are treated as point particles, are assigned a positive or negative magnetic polarity, and undergo clustering or cancellation when they come within an interaction distance $d_i = 0.34$ Mm of one another. Solar-like differential rotation and poleward meridional flow are also included and contribute a temporally steady displacement of tubes and clusters. Individual tubes are injected randomly all over the photosphere, while tubes and clusters undergo random submergence at a size-dependent rate. In Crouch et al. (2007) the various parameters in this model were adjusted to yield a best fit to the observed spatial distribution and probability density function of magnetic flux; these optimal parameter values also yield a flux reprocessing time in the quiet Sun commensurate with observations, even though this quantity was not used to constrain the fit (see Paper I, §2.2, for further discussion).

As in Paper I, the simulations reported upon herein also include the injection of magnetic flux in the form of active regions. We opted to use the Wang and Sheeley sunspot database for cycle 21, which covers emergences from 1976 August 16 to 1986 April 5, for 9.63 years worth of data. All the active regions with unsigned flux $\geq 2 \times 10^{20}$ Mx that emerged during that cycle were included, with their time, latitude and longitude of first appearance, maximum (initial) magnetic flux and —importantly for our purposes— polarity of leading spot (see Fig. 1). There are 3047 such entries in the database.

Injected sunspots undergo decay through boundary erosion, releasing elementary flux at a rate proportional to their radius (see Paper I, §2.3). These are carried radially away from the spot by a specified moat flow, as they gradually begin their random walk and interaction with other tubes and aggregates. This procedure is equivalent to a sunspot disintegration rate proportional to A/T, where A is their maximum area and

T their lifetime, in agreement with the Gnevyshev-Waldmeier law (see Petrovay & Van Driel-Gesztelyi 1997; also eq. (4) of Paper I). This boundary erosion process operates until all the spot's magnetic flux has been released as elementary tubes.

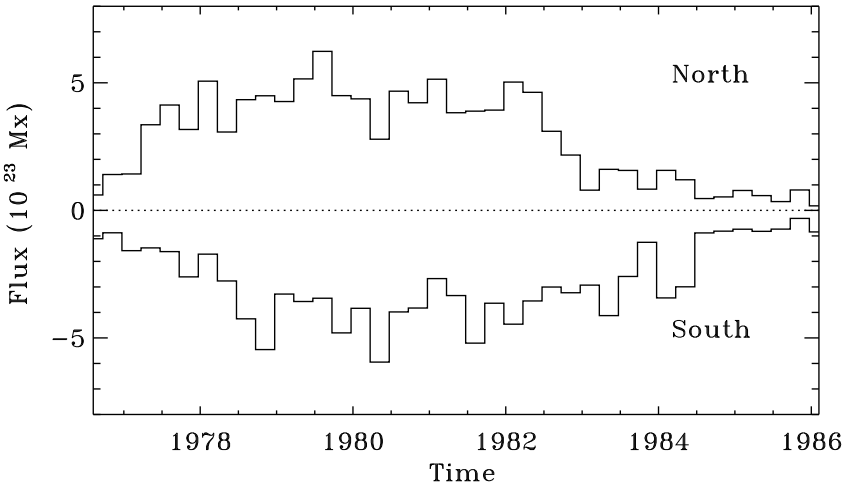

Fig. 1.— Unsigned flux injection from active regions per trimester for cycle 21, from the Wang and Sheeley active region database. For the purpose of this plot, the Southern hemisphere unsigned flux is (arbitrarily) plotted as negative. The surface flux evolution throughout cycle 21 has been extensively analysed and modeled by these authors (Wang & Sheeley 1989, 1991, 1994; Wang et al. 1989a, 1989b, 2002), and so allows a detailed testing and validation of our own modelling approach. The first cycle 21 active region appearance is on 1976 August 16, and the last takes place on 1986 April 5. The total unsigned magnetic flux injected in the Northern and Southern hemisphere is 1.10×10^{25} Mx and 1.08×10^{25}, respectively.

Our Monte Carlo surface flux evolution model represents an extreme simplification of the magnetohydrodynamical (MHD) processes driving solar photospheric magnetic flux evolution. With the modelled system spanning some five orders of magnitude in length

scale, six orders of magnitude in timescale, and six orders of magnitude in magnetic flux scale, a formal MHD treatment is clearly ruled out. Even our highly simplified model remains computationally challenging. The simulations typically involve the tracking of $N_t \sim 10^7$ flux tubes at any given time, every pair of which needing to be tested for interaction with neighbours at every time step, during $\simeq 2 \times 10^5$ time steps. The direct approach, calculating each pair of distance, scaling as N_t^2 would be clearly impractical (as well as wasteful).

We opted to make use of a tiling algorithm appropriate for N-body simulations (Allen & Tildesley 1990; Mattson & Rice 1999), which leads to order-of-magnitude savings in computing time. To find interactions between flux tubes we loop only over neighbouring tiles within the interaction distance. The tile size is chosen as a function of the interaction distance and the number of flux tubes in the simulation to minimize the computing time. The number of tiles per latitude band varies from the equator to the poles, with only one tile at each pole (Figure 2).

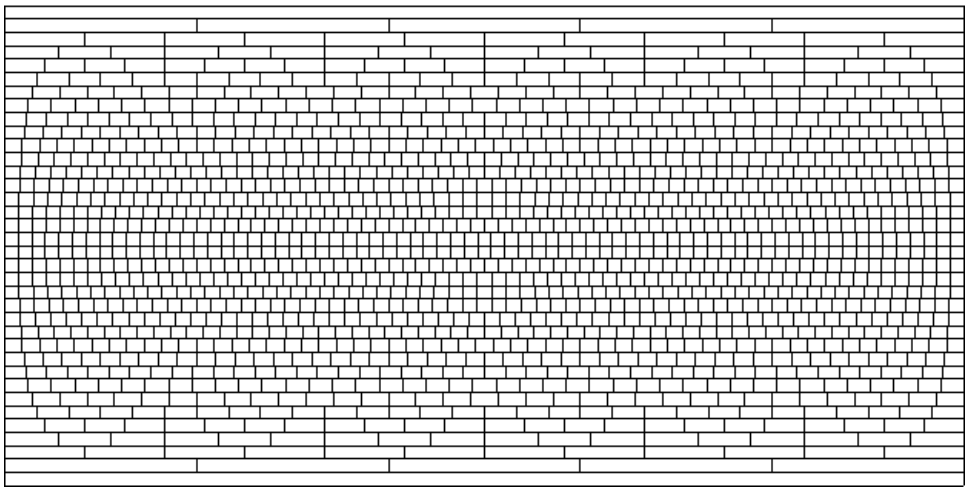

Fig. 2.— Subdivision of the simulation domain with tiles, shown on a latitude-longitude projection.

Flux tubes are stored in linked lists according to the tile where they belong and their polarity, to avoid testing for cancellation of same-polarity tubes or clustering of opposite-polarity tubes. A further optimization that greatly reduces the simulation time is the merging of same-polarity flux tubes in a special cluster considered as a particle when the distance between the tubes gets smaller than 0.01 times the interaction distance. The polarity of this cluster is simply the sum of the fluxes of the merged tubes. We limit the number of flux tubes that can thus merge to 100. The interaction algorithm starts by merging flux tubes of the same polarity, then it proceeds with cancellation of flux tubes of opposite polarity within the interaction distance. Finally, it creates clusters with remaining tubes of the same polarity within the interaction distance. Even with these optimizations, one time step ends up requiring $\simeq 2.5$ core-minutes, adding up to 1.5 core-years for the cycle-length simulations discussed in what follows.

3. Simulated evolution of the magnetic cycle over cycle 21

3.1. Simulation design

The simulations discussed in what follows represent the extensions to solar cycle timescale of the three reference simulations discussed in Paper I (see also Table 1 herein). Simulation 1 incorporates only spatially and temporally uniform injection of individual flux tubes. The statistically stationary state of this simulation thus represents a true quiet Sun, i.e., one that has never experienced the emergence and decay of active regions. Simulation 2 injects magnetic flux only as sunspots according to Wang and Sheeley's sunspot database for cycle 21. Unlike simulation 1, here magnetic flux injection occurs across a range of flux scales, in a spatiotemporally intermittent manner, and at an overall rate also varying slowly in time (viz. Fig. 1). Those sunspots then disintegrate into individual flux tubes. Simulation 3 combines injection of sunspots at large scales with injection of elementary

flux tubes at small scales. The numerical parameters controlling the displacement and interaction of magnetic elements are the same in all three simulations, and set at the scaled-up best-fit values established by Crouch et al. (2007; see also Table 1 in Paper I, and discussion therein of the scaling-up procedure).

Table 1: Simulation results after 3 yr

	Injection	PDF slope	Fractal dimension	Initial condition
Parnell et al. (2009)	(Real Sun)	-1.85 ± 0.14	—	
Crouch et al. (2007)	Flux tubes	-2.3	1.70	
Sim 1	Flux tubes	-2.10 ± 0.06	1.70	Unmagnetized photosphere
Sim 2	Active regions	-1.31 ± 0.04	1.66±0.004	Unmagnetized photosphere
Sim 3	Flux tubes + active regions	-1.69 ± 0.02	1.69±0.002	Equilibrium state of Sim 1

Simulation 3 turns out to be the best of the three, in terms of simultaneously reproducing the observed power law slope of magnetic flux distribution, as well as the observationally-inferred fractal dimension of large network elements. It is also, in principle, the most realistic of our three global simulations, in the sense that flux injection takes places over a wide range of scales, although intermediate injection scales, associated e.g. with ephemeral active regions, are not included. Most results discussed in what follows pertain to this simulation, unless explicitly noted otherwise.

3.2. Surface magnetic flux evolution

Figure 3 shows a modeled magnetogram of the surface flux buildup in simulation 3, in which magnetic flux emergence occurs through the injection of both active regions and individual flux tubes. The five frames are taken two years apart, spanning activity cycle 21, with the full latitude-longitude computational plane displayed here in Mollweide projection. Active regions begin appearing at mid-latitudes by t=1 yr (first panel). The largest aggregates forming poleward of the activity belts from the decay of active regions reach a size sufficiently large that they persist long enough to be carried poleward by meridional circulation. By t=3 yr (second panel), some of these clusters have reached the polar regions. Because the surface meridional flow is poleward-directed, equatorial regions remain mostly cluster-free in the early part of the cycle. As the cycle unfolds and active regions emerge progressively closer and closer to the equator, aggregates start to populate that region (third panel). Most longer-lived, large clusters remain until the seventh year (fourth panel). By the ninth year (fifth panel), most large clusters have disappeared from the mid-latitudes, but some survive in polar regions, as well as low latitudes, building up in response to the decay the few active regions emerging in the late phase of the cycle.

Figure 4A shows the modeled evolution of unsigned hemispheric fluxes (dotted lines), along with total signed magnetic flux across the computational plane (solid line), over the duration of cycle 21. Recall that simulation uses as its initial condition the "quiet Sun" equilibrium state of simulation 1, which is characterized by a total unsigned magnetic flux of 4×10^{23} Mx. Around the activity maximum in 1981, the global unsigned flux in simulation 3 has increased by an order of magnitude, up to almost 4×10^{24} Mx. Now, given our flux tube injection rate, the entire cycle 21 has undergone the injection of 1.5×10^{27} Mx in elementary flux tubes, while active regions provided only 2.2×10^{25} Mx, two orders

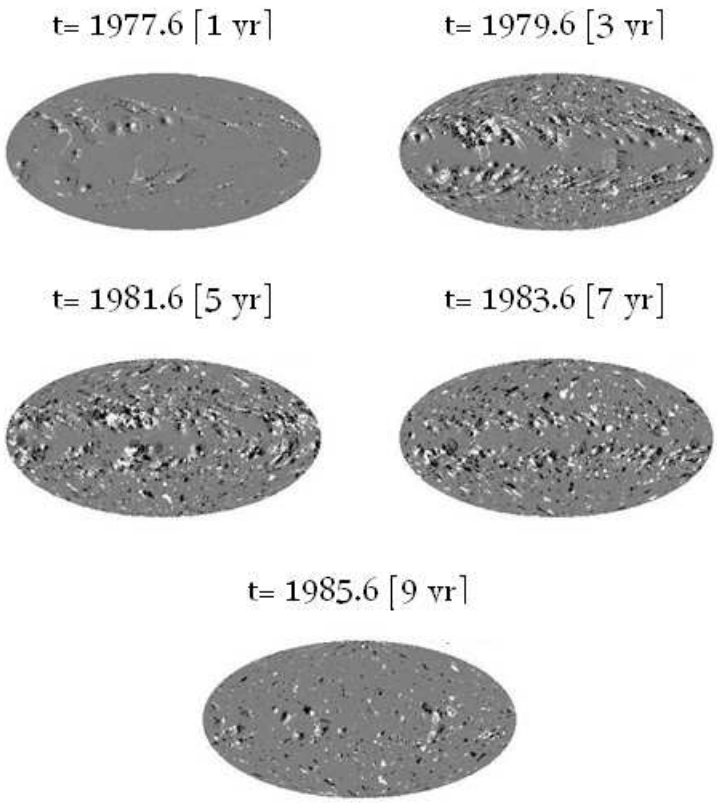

Fig. 3.— Surface evolution of magnetic flux following the injection of active regions from the Wang & Sheeley database for simulation 3. Time zero corresponds to 1976 August 16, marking sunspot minimum between cycles 20 and 21. Each frame shows a pixellized snapshot in Mollweide projection of the magnetic flux in the computational plane, spaced two years apart and spanning cycle 21. Aggregates forming from the decay of active regions are transported poleward by the meridional flow, and sheared horizontally by differential rotation. Note also how large bipolar active regions emerging at mid-latitudes nearly all show the same ordering of magnetic polarity with respect to the longitudinal direction, negative (black) leading positive (white) in the Northern hemisphere, and opposite in the Southern hemisphere; this is a reflection of Hale's polarity laws.

of magnitude lower. Notwithstanding the challenge of observing $\sim 100\,\mathrm{km}$ wide structures carrying a $\sim 10^{16}\,\mathrm{Mx}$ flux, observational analyses suggest an even larger contribution of the internetwork, possibly going as high as four orders of magnitude over the contribution of active regions over an eleven-year solar cycle, especially if transient horizontal magnetic fields are included in the flux budget (de Wijn et al. 2009, Ishikawa et al. 2010). Nonetheless, the total unsigned flux in simulation 3 is very similar to that measured in simulation 2 (not shown). This suggests the main contribution to the total unsigned flux comes from the injection and decay of active regions. While this may seem contradictory with the two orders-of-magnitude discrepancy between the amount of flux injected through sunspots and individual flux tubes, it can be explained by the lifetime of small flux concentrations being a lot shorter than that of the large ones. Moreover, Crouch et al. (2007) could show that in their local version of our simulation 1, the vast majority of injected elementary flux tubes disappear through cancellation with a tube of opposite polarity, rather than disappearing "spontaneously" via the probability test mimicking the effects of convective submergence (see their §3.1).

The global photospheric signed flux stabilizes around $+1.4 \times 10^{23}\,\mathrm{Mx}$, comparable to the Southern hemisphere value $+1.7 \times 10^{23}\,\mathrm{Mx}$, after the end of sunspot injection in March 1986. This global flux imbalance, non-physical as per the solenoidal constraint $\nabla \cdot \mathbf{B} = 0$, arises as a consequence of the statistical procedure used to reproduce convective submergence. In the late phases of the simulation the signed flux is dominated by a small population of large, long-lived clusters of mixed polarity (more on these in §4 below). At each simulated time step, the probability tests that govern the disappearance of these clusters are performed independently for each cluster, so it is entirely conceivable that the loss of one, large unipolar cluster suddenly leads to a net global signed flux of the opposite polarity, which will persist until a comparably large cluster of opposite

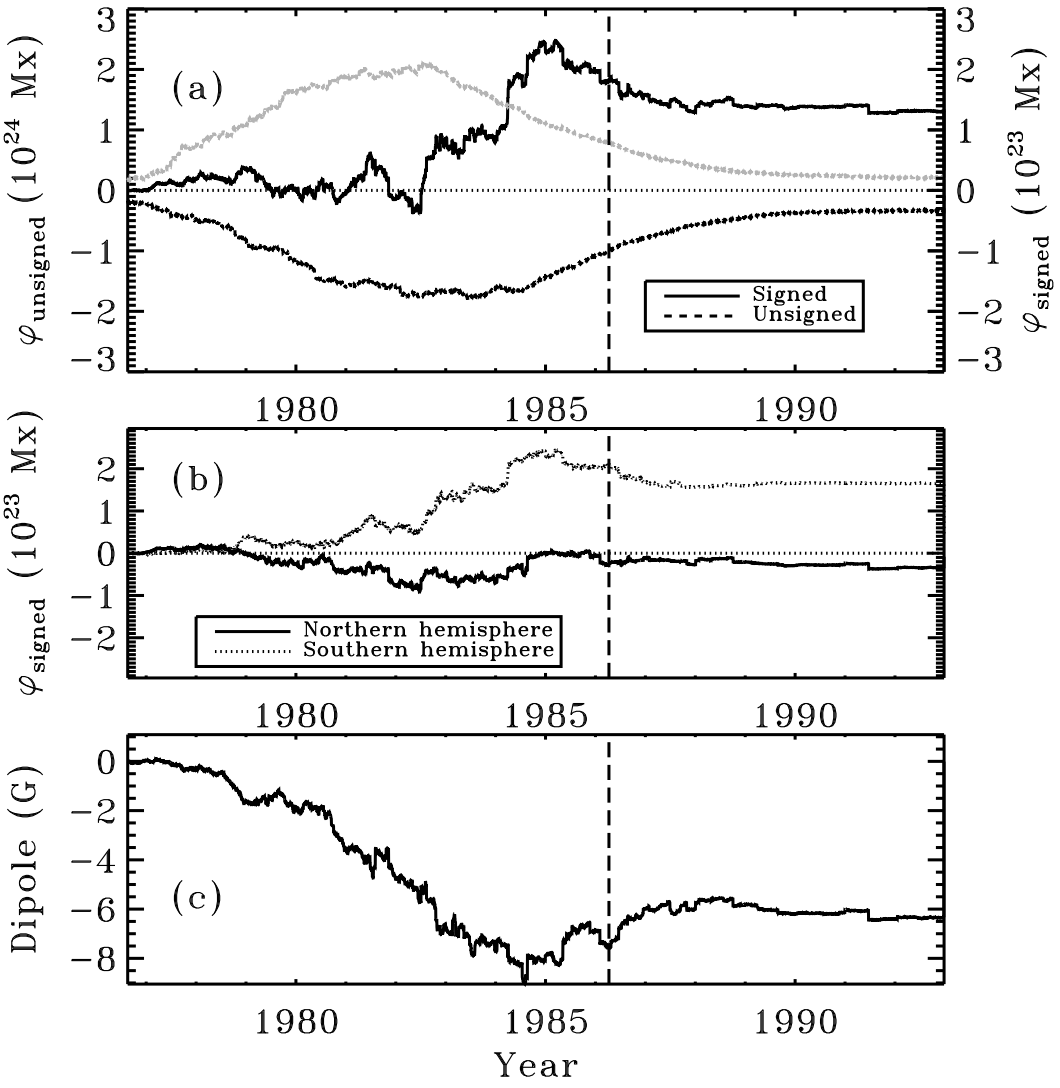

Fig. 4.— Simulation 3 : (a) Total signed (full line) and hemispheric unsigned (dotted line, grey for North hemisphere, black for South) magnetic fluxes. South-hemisphere unsigned flux plotted as negative-valued, as on Figure 1. (b) Hemispheric signed flux over the course of the simulation: North hemisphere (full line) and South hemisphere (dotted line). (c) Dipole magnetic field strength. The vertical dashed line indicates the time of sunspot minimum delineating cycle 21 from cycle 22. The various time series stabilize following the last injection on 1986 April 5. The intermittent abrupt variations are due to the disappearance of a large cluster.

polarity vanishes in turn. In other words, our injection processes generate no net flux, our cancellation procedure respects flux balance, but the "submergence" mechanism built into the simulation does not. Note however that net signed flux imbalance at the end of the cycle remains quite small, at the 0.1 % level, compared to the total unsigned flux injected in the simulation throughout the cycle. Flux imbalance at this level is insignificant with regards to the evolution of the network properties that are the focus of this Paper.

Even though the last spot injection is taking place on 1986 April 5 in the Wang & Sheeley database, we continued running the simulation all the way to 1993, without injecting any cycle 22 active region. This procedure thus allows us to measure the system's relaxation time, a topic to which we shall return in §5 below. At this juncture, note simply on Figure 4A how the photospheric unsigned flux is still decreasing towards its initial "quiet Sun" value, more than 4 years after the end of sunspot injection, indicative of persistence of network elements on long timescales.

A well-known observed property of emerging large bipolar active regions is the systematic pattern of average tilt with respect to the E-W direction of the line segment joining the center of each member of the pair, with the leading member of the pair (with respect to the direction of rotation) being usually located closer to the equator than the trailing member, and the associated tilt angle increasing with heliographic latitude. This statistical pattern is known as Joy's Law, and is now believed to reflect the action of Coriolis force on the flow developping along the axis of the rising magnetic flux ropes forming bipolar active regions upon emergence through the photosphere (Fan 2009). In conjunction with Hale's hemispheric polarity rule, this tilt also implies that upon decay, the decay products of the leading members are more likely to undergo cross-equatorial diffusive cancellation with the leading polarity decay product of bipolar active regions emerging in

the other hemisphere. The net effect is the buildup of a signed hemispheric flux having the polarity of the trailing members of the bipolar active regions in each hemisphere. This phenomenon also materializes in our simulation, as already evident on Figure 4B. Transport and accumulation of the decay products to high latitudes can then lead to the buildup of a dipole moment, and reversal of the Sun's surface magnetic dipole moment having built up in the preceeding cycle (Babcock 1961; Leighton 1969; Wang & Sheeley 1989). This forms the basis of the so-called Babcock-Leighton solar cycle model (Charbonneau 2010).

Our initial condition is such that the initial dipole field strength is originally (and unrealistically) zero. As shown on Figure 4C, simulation 3 generates a dipole of strength -7 G by the end of the cycle, increasing to stabilize at -6 G thereafter (recall that we do not inject cycle 22 active regions). This buildup of a negative dipole moment compares favorably with that modeled by Wang & Sheeley (1991) who find that the dipole went from 3 G to -4 G during cycle 21. As another point of contact with the simulation of Wang & Sheeley (1989, 1991), we can estimate a diffusion coefficient from the random walk step length and time steps used in our simulations. With these parameters set at d_w=$\sqrt{3}$ Mm and Δt=30 minutes respectively in simulation 3, the implicit diffusion coefficient is $D = d_w^2/4\Delta t = 416$ km^2 s^{-1}. This is compatible with the value D=600 $\pm$ 200 km^2 s^{-1} used in Wang et al. (1989b)'s advection-diffusion flux evolution model, confirming that our stronger 1986 dipole results directly from our dipole-free initial condition.

Figure 4A, showing the evolution of total signed and hemispheric unsigned flux, can be compared to Fig. 3 of Schrijver & Harvey (1994). They observe from 3 to 9×10^{23} Mx of total photospheric flux from the 1976 minimum to the activity maximum, whereas we have from 5 to 40×10^{23} Mx for the same times. The flux they measure at the 1986 minimum is the same as during the 1976 minimum. We, on the other hand, do not recover the initial

flux due to certain large persistent flux concentrations. However, Schrijver & Harvey (1994) have a detection threshold of 8×10^{19} Mx, compared to our magnetic unit of 10^{17} Mx, so they excluded a large amount of smaller magnetic flux concentrations that would have otherwise increased their total unsigned flux. Wang & Sheeley (1989) find a variation from 18×10^{23} Mx in 1977 to 36×10^{23} Mx in 1979 to 4×10^{23} Mx in 1985 for bipolar magnetic regions of at least 3×10^{20} Mx. This is comparable to the total (N+S hemisphere) unsigned flux at cycle peak in our simulation. Our higher flux in the late phases of cycle 21 is likely caused by the absence of a polar sink. The extra flux does not influence the index of the flux distribution (see Section 5), only its offset from the origin, as flux processing by surface flows operates on all scales.

3.3. Magnetic flux distribution

Our simulation yields not only the evolution of the total magnetic flux, but also the evolution of the size distribution of the magnetic flux contained in the various clusters populating our computational domain. As shown on Figure 5, this size distribution takes the form of a power law, with index -1.69. Both the power law form and index compare favorably to the flux distribution inferred observationally by Parnell et al. (2009), who find a power law index -1.85 ± 0.14.

Paper I showed that the form of this flux distribution is set primarily by the surface processes of diffusion-limited aggregation, which rapidly erases the "memory" of the flux injection scale(s). Even when working with two extreme flux injection scenarios —simulation 1 with injection of elementary flux tubes only, or simulation 2 with injection of active regions only,— power law distributions spanning many orders of magnitude in magnetic flux build up in less than one year of simulation time. These analyses lumped

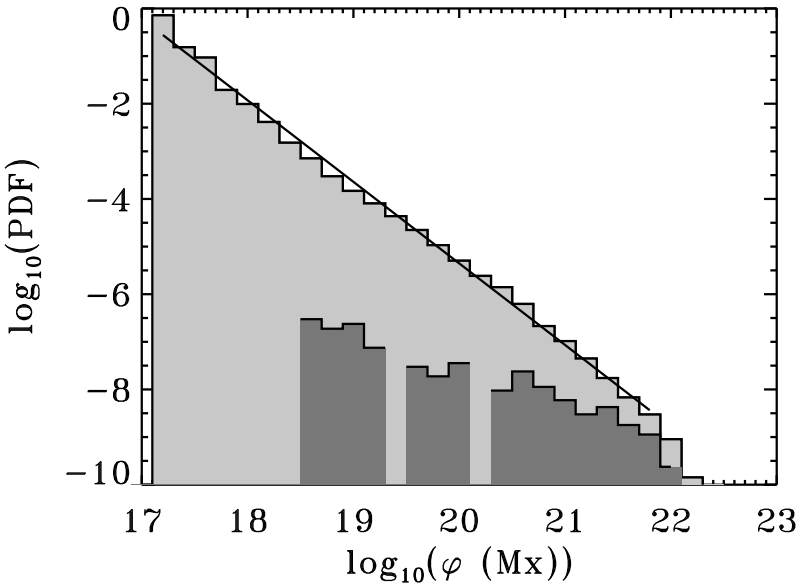

Fig. 5.— Power-law distribution of unsigned magnetic flux for all photospheric magnetic structures present in simulation 3 at t=3 yr after the beginning of cycle 21. The darker histogram isolates the contribution of decaying sunspots to the distribution. The largest sunspot present in the Wang & Sheeley cycle 21 database carries an unsigned flux of 7×10^{22}Mx, and appears on 1982 June 15.

together all magnetic structures present on the simulation domain at a given time. We now refine the analysis by examining the latitudinal and temporal variations of network characteristics.

3.4. Network magnetic flux

We henceforth focus on the magnetic network building up in our simulation 3. Our first task is to define criteria that will allow us to select which clusters are considered part of the network. We obviously do not include decaying spots, nor should we include

individual elementary flux tubes continuously injected in the domain. Following Crouch et al. (2007), we define network elements as clusters containing 10 or more elementary flux tubes. The associated magnetic flux, 10^{18} Mx, is comparable to the threshold used in observational studies to distinguish the network from the so-called inter-network magnetic flux concentration, although the distinction is arbitrary to some significant degree (see Stenflo 2013, and discussion therein). In simulation 3, the network elements so defined collectively carry between 1.3×10^{23} Mx and 34×10^{23} Mx at its peak coverage, amounting to 95 % of the total photospheric unsigned flux.

3.5. Network filling factor

The photospheric network coverage is expressed as the filling factor, which is the area occupied by clusters of flux tubes (excluding spots), over the total area under study. With the cross-sectional area of our elementary flux tubes set directly by our adopted values for their associated magnetic flux ($\Phi_t = 10^{17}$ Mx) and assumed (vertical and uniform) field strength $B_t = 1000$ G, it is straightforward to compute a photospheric filling factor by simply multiplying the equivalent area $A_t = \Phi_t/B_t = 10^{-2}$ Mm^2 by the total number of flux tubes. The absolute values of the filling factors so computed will end up scaling inversely with the chosen value for the magnetic flux density B_t; however, the relative variations of the filling factor with latitude and phase of the cycle, which are the focus of the foregoing analysis, remain independent of this choice. We note that for a 1 kG field strength the "diameter" of our elementary tubes is $D \simeq 113$ km, comparable to the current resolution limits of magnetographic observations (see Stenflo 2013 for further discussion).

We first segment our spatial domain in latitudinal strips of angular width $\Delta\theta = 5°$,

so as to extract the variation of the network filling factor in latitude and time. Figure 6 shows the latitudinal distribution of the network filling factor at 4 successive epochs during cycle 21, spaced two years apart. The solid line is the latitudinal distribution characterizing Simulation 1, i.e., without active region injection but otherwise identical in its parameter settings, which is used here as the initial condition. The latter only shows a very mild increase of the filling factor with increasing latitude, hardly visible on the scale of this plot. This may appear surprising, as the poleward meridional flow is inexorably leading to the accumulation of tubes and clusters at high latitudes. However, the increased proximity of clusters and tubes, being gradually concentrated in the small surface of the polar cap, also increases the probability of tubes and clusters disappearing by cancellation with tubes and clusters of opposite polarity. On the other hand, as we shall see presently, in the presence of a net signed flux this proximity will also favor the formation of large, persistent unipolar clusters, given that our submergence probability decreases with cluster size.

The dotted, dashed, dash-dotted and long-dashed distributions are extracted 1, 3, 5, and 7 years following the beginning of cycle 21, and correspond to the first four panels of Fig. 3, for the simulation with the network and active regions. As expected, the network filling factor increases rapidly at mid-latitudes during the rising phase of the cycle, in response to the emergence and decay of active regions. The equatorial latitudes are lagging behind, due to the paucity of low-latitude emergences in the early phases of the cycle, and the poleward advection of mid-latitudes magnetic structures by the meridional flow, which partly offsets the random walk of tubes and clusters towards equatorial regions. Even in the late phases of the solar cycle, the increase of the network filling factor at equatorial latitudes remains modest, by about a factor of three over the initial condition. At high latitudes, on the other hand, poleward advection by the meridional flow leads to a large increase in filling factor, starting after about 2 years and already reaching a factor of ten three years after cycle onset.

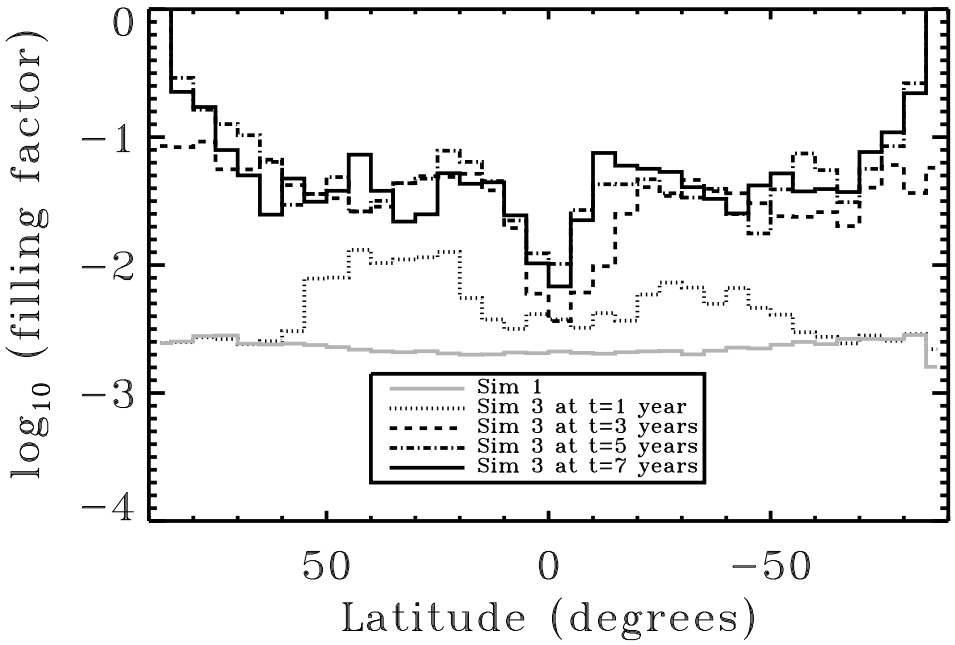

Fig. 6.— Latitudinal distribution of magnetic filling factor for simulation 3 after 1 year, 3 years, 5 years and 7 years since the beginning of cycle 21. The solid line shows the (statistically stationary) latitudinal distribution for simulation 1, which does not include injection of active regions. The small increase of the high latitude filling factor characterizing simulation 1 reflects the inexorable poleward transport by the meridional flow (see text).

The filling factor becomes sharply peaked at polar latitudes in the descending phases of the solar cycle, reaching values almost two orders of magnitude higher than in the spot-free simulation used as initial condition. This occurs because the decay of active region by boundary erosion tends to produce larger clusters (i.e., comprised of more than 10^4 elementary tubes) than does random injection of individual tubes all over the surface. Such large clusters have longer lifetimes and consequently are more likely to survive long enough to be advected by the meridional flow all the way into polar regions. In our simulation, clusters have a life expectancy scaling as $\tau\sqrt{n_e}$, with τ=6.9 d being the lifetime parameter and n_e the number

of elementary flux tubes in a cluster. For a 10^4-tubes cluster (carrying a 10^{21} Mx flux), the life expectancy reaches 2.0 years, which is a significant fraction of the cycle duration and commensurate with the advection time from low to polar latitudes. Our simulation has generated 491 such clusters after 5 years. Moreover, while the simulation incorporates a form of convective submergence via the lifetime parameter, global subduction of tubes and clusters by the meridional flow at high latitude is not included here. Such subduction, if it does take place, would lead to a significant reduction of the filling factor in polar regions.

Figure 7 shows the variation of the latitudinally-integrated filling factor versus cycle phase, the latter measured here via the amount of active region flux injected as a function of time (viz. Fig. 1). The filling factors are taken and injected flux values summed over successive, contiguous three-month blocks, successive blocks being joined by a line segment, with the cycle unfolding here in a counterclockwise direction. The loop-like path traced in the course of the cycle indicates that the network filling factor is not simply set by the instantaneous rate of flux emergence, but instead exhibits a significant "memory" of past emergences, primarily via the long lifetimes of large clusters. Our model therefore predicts a complex dependence of the network filling factor on cycle phase and latitude, characterized by a latitude-dependent temporal lag.

Figure 8 shows a synoptic map of the filling factor for the whole cycle 21 and the following extended time period during which the simulation was pursued without the injection of any cycle 22 active regions. The grey scale saturates at a filling factor value of 0.2. The inclined streaks are associated with large clusters, forming at active regions latitudes from the decay of the injected active regions, carried to high latitudes by the surface meridional flow. Once active region injection ceases (vertical dashed line), the filling factor rapidly drops, except at polar latitudes, and for the drifting trace of a few large clusters formed at the end of the

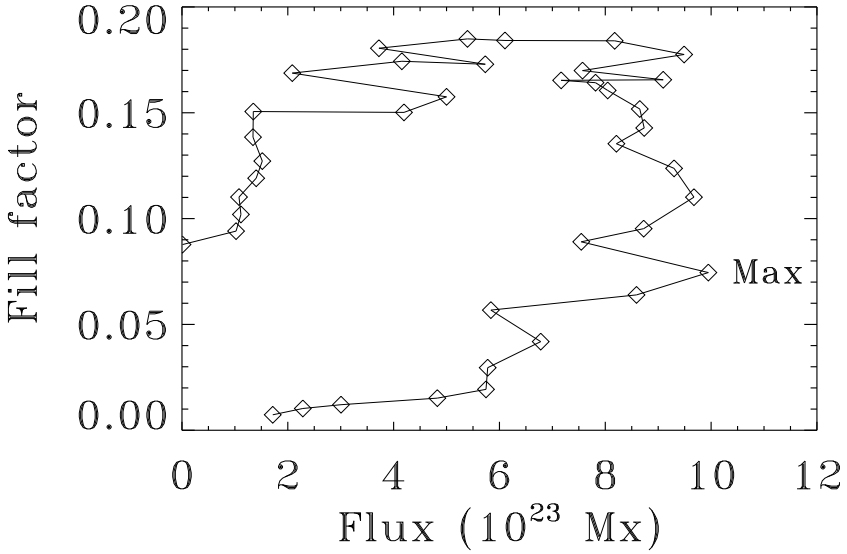

Fig. 7.— Three-month samples of the filling factor vs summed injected flux in simulation 3. The cycle unfolds in a counterclockwise direction on this plot, starting in August 1976 in the bottom left corner, with the trimester at which activity maximum occurs also indicated. The curve does not return to the origin because of the remaining large clusters' contribution to the filling factor at the end of the simulation.

cycle near the equator.

Although the distinction carries some arbitrariness (Stenflo 2013), an attempt can be made to distinguish the network from the so-called inter-network, referring to the small magnetic flux concentrations omnipresent on the quiet Sun, away from granular cell boundaries. Here we can assign network versus inter-network status simply on the basis of magnetic flux, the latter including all structures with flux smaller than 10^{18} Mx, a value comparable to the 2×10^{18} Mx used by Wang et al. (1995) as the flux threshold in their observational analysis. Our inter-network so-defined carries an unsigned flux of 1.1×10^{23} Mx, a value remaining essentially constant throughout our simulated cycle 21, in contrast to the network unsigned flux which increases markedly as the cycle unfolds. At

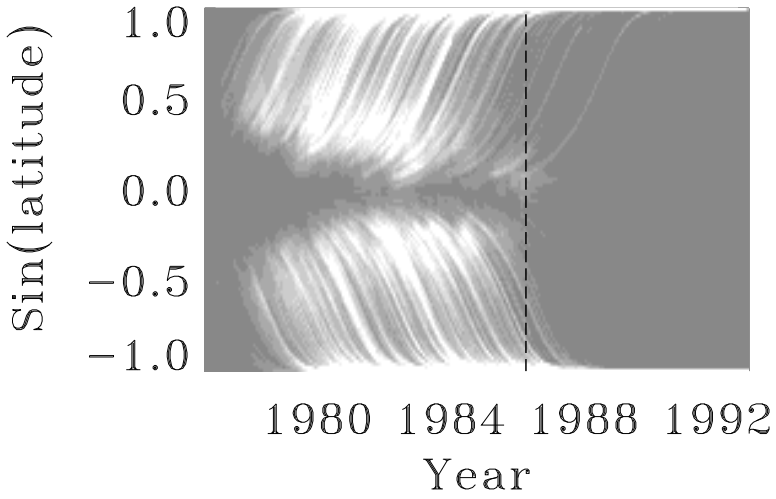

Fig. 8.— Synoptic map of the filling factor, saturated at 0.2, for simulation 3. Sunspot injection ceases at 1986 April 5, the end of cycle 21, with no cycle 22 active regions being injected thereafter. The vertical dashed line indicates the time of sunspot minimum delineating cycle 21 from cycle 22.

cycle maximum, the peak of cycle 21, our simulations yield an inter-network to network ratio of magnetic flux equal to 35%, significantly smaller than the 41% characterizing reference simulation 1, which excludes injection of active regions; this confirms that the injection and subsequent decay of active regions favors the formation of larger clusters of elementary flux tubes. Since this simple calculation distinguishes inter-network elements only on the basis of magnetic flux value and not spatial location, it is expected that the ratio so obtained be higher than the 20 % determination of Wang et al. (1995). Nonetheless, our simulation results certainly remain consistent with the notion that a large fraction of photospheric magnetic flux resides in the inter-network, and is largely independent of cycle phase or amplitude.

Overall, our filling factor values stand at the upper end of observational determina-

tions for the solar photospheric network (cf., e.g., Orozco Suarez et al. 2007, Ishikawa & Tsuneta 2009). Recall however that our simulations are formulated in terms of elementary magnetic flux carrying a flux of 10^{17} Mx, and thus that the basic scale of our filling factor calculation is entirely set by the (uniform) 1 kG field strength assigned to our elementary flux tubes; our filling factor values thus scale inversely with this assumed field strength. What remains independent of this assumption is the *relative* variation of the filling factor with latitude and/or time, which can thus be considered a robust result.

3.6. Inter-cluster distance

Inter-cluster distance is calculated by computing the distance to each cluster's ten nearest neighbors, and by averaging these ten measurements. As demonstrated in Crouch et al. (2007, §3.5), this very simple procedure yields results that compare well with more involved (and computationally expensive) techniques, such as Voronoi tessellation or spectral methods. In the following analysis, square patches of 100 Mm side are sampled at one-month cadence, set at various latitudes. The monthly evolution of average inter-cluster distance is shown in Figure 9 for latitudes 0°, 15°, 30°, 45° and 60°. This quantity remains remarkably steady, fluctuating around 20 Mm for all of the activity cycle at most of the latitudes, and decreases slightly with increasing latitude at most phases of the cycle. Some temporal variations are observed at active region latitudes as the cycle unfolds, in the form of a mild increase of the inter-cluster distance during a ~ 3 yr time interval centered on cycle maximum. Intercluster distance in our simulation does not seem to be otherwise affected by sunspot activity. This suggests that the mechanism responsible for establishing the characteristic length scale in the spatial distribution of network elements depends

mainly on the injection rate of elementary flux tubes, at least away from active latitudes.

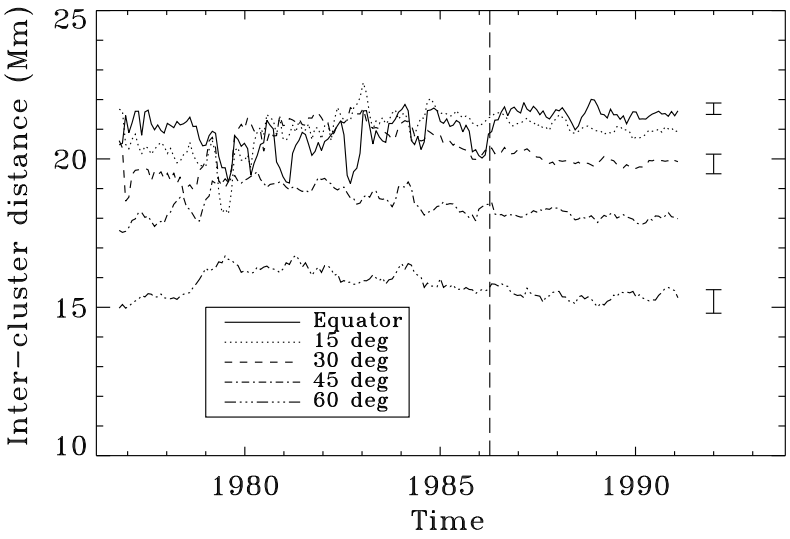

Fig. 9.— Monthly evolution of inter-cluster distance for simulation 3 at five latitudes: straddling the equator (solid line), 15° (dotted line), 30° (dashed line), 45° (dot-dashed line) and 60° (triple dot-dashed line). The time series plotted are box-car averages of 5-month width. Error bars are shown for the equator, 30° and 60°. The vertical dashed line indicates the time of the last active region injection for cycle 21. Note that the inter-cluster distance stabilizes after the last injection.

In the following discussion, we use inter-cluster distance as a proxy for supergranule size. We will restrict our analysis to simulation 3. The range of observed supergranule sizes lies between 12 and 75 Mm (Rieutord & Rincon 2010), with values around 30 Mm most often quoted as peak or mean of the distribution. Our values fall within this range, at around 20 Mm, with a decrease to ~ 16 Mm at high latitude. Here this decrease is a direct consequence of the poleward meridional flow, which inexorably decreases the distance between neighbouring clusters. Qualitatively, this trend is consistent with the analysis of

Raju et al. (1998) who also find a dependence of supergranule diameter with latitude at different activity minima, with a broad minimum around 20° N, however with a measured average supergranule diameter of 32 ± 1 Mm.

The cycle-trend produced by our simulation at 30° latitude is qualitatively similar to the observational trend inferred by McIntosh et al. (2011) for cycle 23, with supergranule sizes increasing with activity from 25 Mm at the minimum to around 30 Mm at the maximum. In our simulation, however, the 2 Mm min-to-max increase is smaller by a factor of two. Note however that these trends stand in opposition to the observational analysis of Meunier et al. (2008), who found instead that supergranular size decreases as activity increases, so smaller supergranules should be seen in activity belts and at activity maximum as opposed to polar regions and activity minimum. Rimmele & Schroter (1989) also found a latitudinal trend in supergranular size at the 1986 activity minimum, cells being some 10% smaller at mid-latitudes than in equatorial regions, roughly consistent with our simulation results although in absolute terms their inferred supergranular diameters are significantly larger (34–38 Mm) than our typical inter-cluster distances.

Srikanth et al. (2000), in their analysis of supergranules, calculated statistical moments of their size distribution. They found a mean supergranular size ranging from 16 to 23 Mm, depending on the data used. Their distribution with the larger mean is characterized by a skewness of 1.1 ± 0.01 and a kurtosis (peakedness) of 4.6 ± 0.09. We find for simulation 3 a skewness fluctuating around 0.5 ± 0.5, implying that our distribution is less asymetric than in Srikanth et al. (2000), but a comparable kurtosis of 5 ± 1. Our standard deviation varies around 9 ± 1. Our skewness, kurtosis and standard deviation do not significantly change over time.

To sum up; despite its simplicity, our network formation and evolution model yields results that compare favorably to a number of observational inferences, including (1) the power-law form and index of the distribution of magnetic flux observed in photospheric structures; (2) their fractal index; (3) the length scale of their spatial distribution, to the extent that our inferred length scales can be compared to the supergranular scale; (4) when applied to cycle 21, and accounting for our field-free initial condition, the buildup of a global dipole component of strength in agreement with observations and other modelling approaches to surface magnetic flux transport; (5) an overall signed and unsigned hemispheric magnetic flux balance also in reasonable agreement with observational inferences and other model calculations. As a further test on the degree of realism in our modeled evolution of the magnetic network, we now turn more specifically to the behavior of the network at polar latitudes, for which recent observations have yielded some remarkable and unexpected results.

4. Polar cap evolution

Because of the combined flux dispersal by surface convection and inexorable poleward advection by the Sun's surface meridional flow, the evolution of polar cap magnetism is closely related to the global evolution of surface magnetism throughout successive activity cycles. From the modelling point of view, this means that any conceptual error or oversimplification in the design of a surface flux evolution model will have a large, cumulative impact in the polar caps. A detailed comparison of model predictions to observed polar behavior thus offers a strong test of the model. In the following we follow Tsuneta et al. (2008) in defining the polar caps as the areas contained above $\pm 75^\circ$ in latitude.

Detection of the Sun's dipole moment goes back over half a century (Babcock

1959), but detailed investigation of polar behavior is a relatively recent endeavour (e.g. Okunev & Kneer 2004, Blanco Rodriguez et al. 2007), and has reached a detailed level with the high-resolution, high-sensitivity spectropolarimetric observations recently provided by the Hinode mission (Tsuneta et al. 2008). Analysis of Hinode data by Shiota et al. (2012) revealed a remarkable and unexpected property of polar cap magnetism, namely the fact that the polar magnetic field is far from uniform and diffuse, but instead is concentrated in a relatively small number of strongly magnetized structures. These polar magnetic flux concentrations are characterized by higher total magnetic flux and average area than their quiet Sun counterparts, and a predominance of one (opposite) polarity in each hemisphere, in contrast to the balanced positive and negative fluxes of the quiet Sun away from active regions. More specifically, Ito et al. (2010) determined the flux in the magnetic concentrations at the poles to be 4.8 times higher than in the quiet Sun at the end of cycle 23 (Ito et al. 2010), with a per-structure average of 2.0×10^{19} Mx.

Figure 10 shows our simulated North pole in simulation 3 at the same 2-yr cadence as on Fig. 3. At $t = 1\,\mathrm{yr}$, the few large clusters having formed from the decay of active regions injected to date in the computational plane in the quiet Sun have not had time to be carried to polar regions by the meridional flow, so that the polar cap remains largely devoid of significant magnetic flux, as per our dipole-free initial condition. Of course, injection of elementary flux tubes takes place in the polar caps as well, which leads to the buildup of clusters of moderate size (reaching a few $10^{19}\,\mathrm{Mx}$), but these are too small and do not carry enough flux to be visible on the grayscale of Fig. 10. The situation is markedly different three years after cycle onset, when larger clusters of either polarity are now present at high latitudes, with some already present in the polar caps. This time lag is consistent with our adopted meridional flow profile. By $t = 5\,\mathrm{yr}$, the polar cap contains many such clusters, packed closely together, which leads to high local filling factor (viz. Fig. 6). However,

this close proximity favors both merging of clusters of similar polarities, as well as erosion and/or fragmentation of clusters of opposite polarities when they collide. Nonetheless, approximately from sunspot maximum (1980) onward, the polar caps are populated with many large clusters of both polarities.

Although one would be hard-pressed to ascertain this visually on Fig. 10, after 7 yr of simulation time the polar cap carries a small, negative signed magnetic flux of a few $\sim 10^{22}$ Mx, falling to a few -10^{21} Mx after 9 yr of simulation. Figure 11 illustrates this evolution of the signed (dotted lines) and unsigned (dashed lines) magnetic flux for the two polar caps. The buildup of a net signed (positive) magnetic flux in the Southern polar cap is more pronounced than in the North, in agreement with the modelling results of Wang et al. (1989a, 1989b) and Schrijver et al. (2002). Except in the early years of the simulation, the polar caps carry an unsigned magnetic flux largely in excess of their respective signed fluxes.

Another fascinating result having come out of vector magnetographic observations by Hinode during cycle 23 is the realization that the largest flux concentrations observed in polar regions carry the bulk of the polar cap's net signed flux. Our modeled polar caps turn out to also show a similar behavior. The solid lines on Fig. 11 show the time evolution of the signed flux associated with the single largest cluster present in each polar cap at a given time. In the Southern hemisphere, this tracks very well the time series of total signed polar cap flux (dotted line), although the match is less impressive in the Northern hemisphere.

At $t = 7$ yr of simulation 3, we get 14 times more flux per polar concentration compared to the quiet Sun instead of the 4.8 found by Ito et al. (2010) for cycle 23.

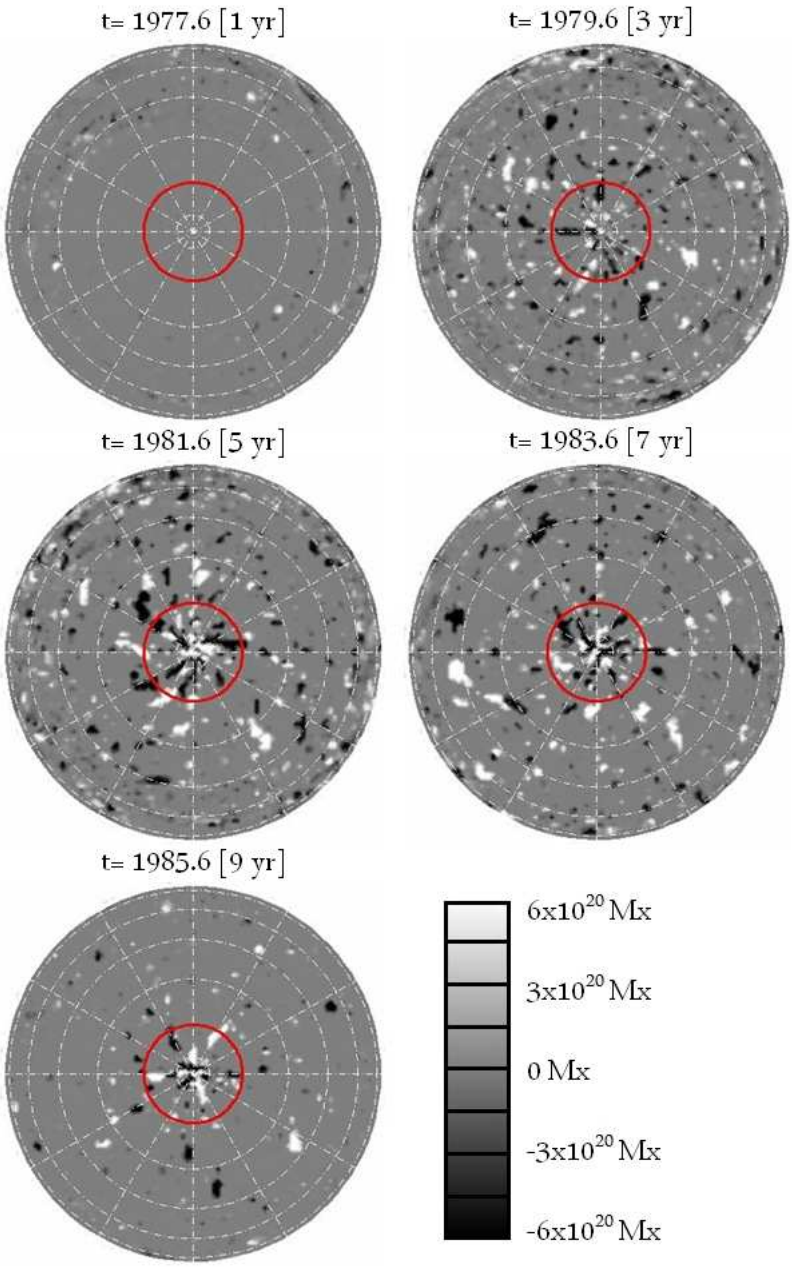

Fig. 10.— Polar view of the Northern hemisphere in simulation 3 at t=1, 3, 5, 7 and 9 yr. The saturation threshold is set at 2×10^{21} Mx per pixel (20 000 flux tubes). The red cirle indicates the 75° latitude used to define the polar cap.

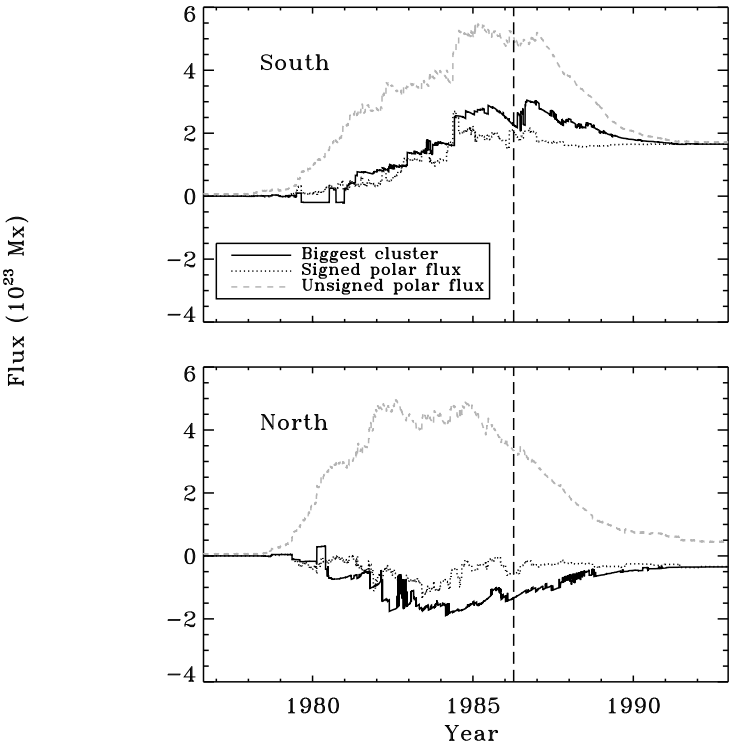

Fig. 11.— Contribution of the largest cluster to the unsigned (grey dashed line) and signed (dotted line) magnetic flux in the Southern (top) and Northern (bottom) polar caps. The solid line on each panel shows the contributions of the largest cluster in each polar cap to the signed flux in that cap. The jumps in those curves are associated with cluster merging and breakup, which can instantaneously change which cluster is being tracked as the largest. The vertical dashed line indicates the time of sunspot minimum delineating cycle 21 from cycle 22.

The higher amplitude of cycle 21 likely contributes to this discrepancy. More important, however, is the lack of a global polar sink in our model, associated with downward entrainement by the meridional flow sinking at high latitudes. As a consequence, our largest aggregates are very large, with fluxes exceeding 10^{22} Mx. The average flux in our polar concentrations is nonetheless 2.37×10^{19} Mx, close to the average determined by Ito et al. (2010). The large amount of smaller concentrations makes our average similar to theirs.

5. Network relaxation time

The recent, unusually extended period of very low magnetic activity observed before the onset of current cycle 24 has lead to the conjecture that the Sun had reached its true magnetic baseline state, where any remaining magnetism is associated exclusively with surface magnetic flux reprocessing. If this is indeed the case, then the observed state of the Sun in the first half of 2009 should have been similar to conditions prevailing during the 1645–1715 Maunder Grand Minimum, offering a much needed window into a magnetohydrodynamical state of the solar photosphere never observed since at least 1913 (see Schrijver et al. 2011, and discussion and references therein). This is particularly germane to the ongoing debate regarding the impact of solar activity on Earth's atmosphere and climate. The key question is: how long does it take for the solar photosphere to lose its "magnetic memory" of a waning activity cycle?

In Paper I we showed that the size distribution of surface magnetic elements established itself quite quickly, from 6 months to a year, independently of the mode of flux injection. This, however, does not automatically imply that this distribution will return to its "quiet Sun" state in a comparable time interval, because of the population of long-lived, large clusters forming in response to the decay of active regions, and accumulating in

polar regions (viz. Fig. 10 herein). Our simulation 3 offers a useful exploratory tool to quantify these effects. Even though the last sunspot appearance in the Wang & Sheeley database occurs on 1986 April 5, we pushed the simulation all the way to the year 1993, maintaining injection of elementary flux tubes everywhere in the photosphere, with the same parameters as before, but *without injecting any cycle 22 active regions.*

Figure 12 shows a time series of sunspot number (in red) and network filling factor for this extended experiment. As noted already in the context of Fig. 7, the network filling factor increases in the rising phase of the cycle, but ends up lagging in phase behing the sunspot number (SSN), with the peak in filling factor occurring in mid-1982, over two years after the peak in SSN. This simply reflects the fact that the largest network clusters build up at high latitude, following their transport and concentration by the meridional flow and diffusive dispersal from active region latitudes.

Figure 12 clearly shows that the network filling factor decreases more slowly than the SSN in the descending phase of cycle 21, a joint consequence of the size-dependent lifetime of clusters built into the model, coupled to the fact that the merging (and thus growth) of existing clusters of the same magnetic polarity is enhanced as they are advected poleward as the cycle unfolds. The SSN minimum between cycles 21 and 22 occurred in March 1986 (vertical dashed line on Fig. 12; see Hathaway 2010). At this point the network filling factor is still almost ten times higher than at the beginning of the simulation, where the initial condition (simulation 1) is a "true" quiet Sun, i.e., having never experienced active region injection. Only by mid-1988, some 2 yr after sunspot minimum, does the network fall back below 50 % of its value at the minimum's onset. Fitting an exponential decay law to the filling factor decrease in the 1985–1990 time interval yields a good fit, with an e-folding time of 2.9 yr. However, removing the contribution of the largest polar clusters ($\Phi > 10^{22}$ Mx),

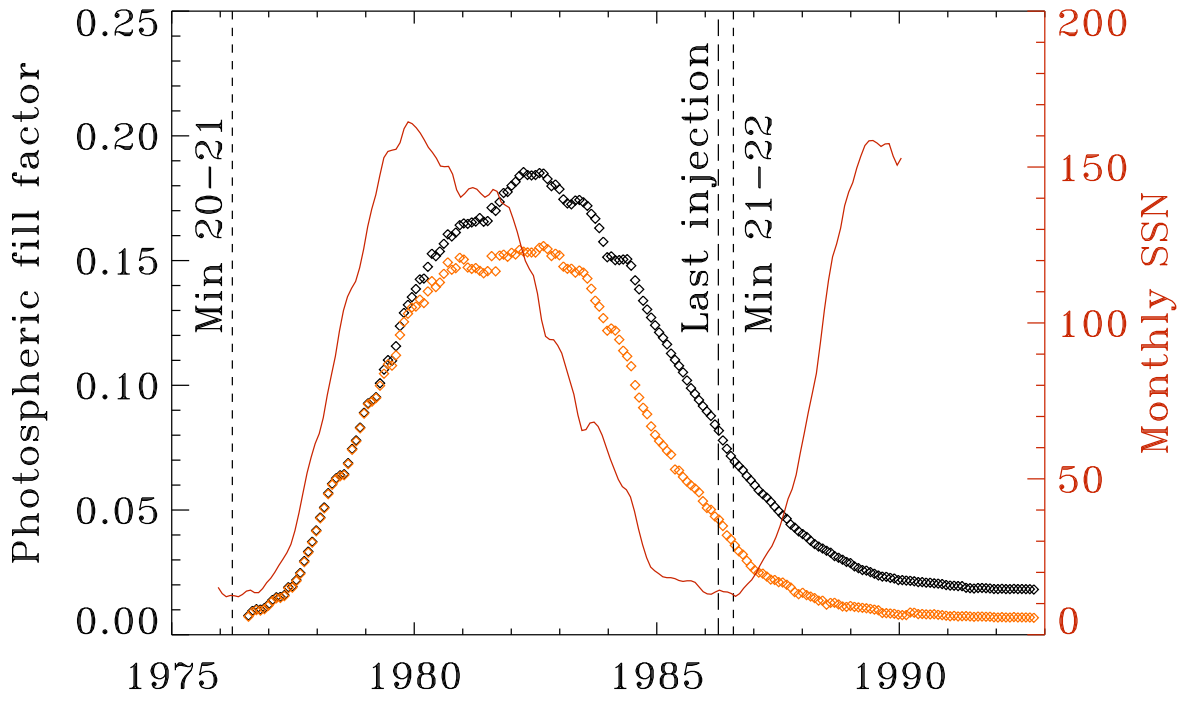

Fig. 12.— Time series of the smoothed monthly sunspot number (red), network filling factor sampled over 3-month blocks (black diamonds), and network filling factor without the contribution of polar clusters of flux larger than 10^{22} Mx (orange diamonds). The two vertical dashed lines indicate respectively the date of last cycle 23 active region emergence, and the SSN minimum between cycles 21 and 22, as labeled. Note the ~ 2.5 yr lag between the peaks in SSN and filling factor, and the slower decrease of the filling factor in the descending phase of cycle 21. Here the last sunspot injection occurred on 1986 April 5, after which no cycle 22 active regions were injected (see text).

the filling factor is only half as much at the minimum's onset, and fitting an exponential decay law in the 1985–1988.5 time interval yields an e-folding time of 1.9 yr.

Figure 13 shows a different view of network relaxation, now in the shape of the distribution of cluster sizes (as measured by magnetic flux), constructed and plotted at a one year cadence starting at the SSN minimum. Here these distributions have *not* been normalized to yield probability density functions, so as to show both the overall decrease in the number of network elements, as well as variations in the shape of the distributions.

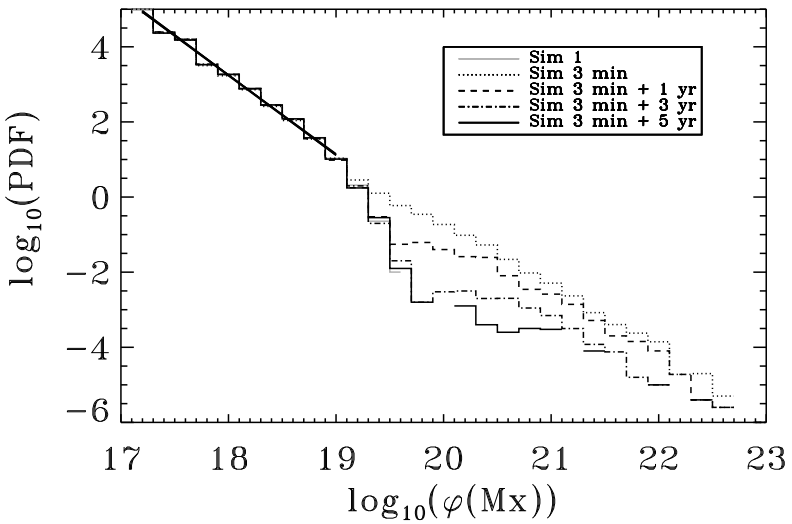

Fig. 13.— Evolving distributions of network cluster flux, extracted at a 1-yr cadence starting at sunspot minimum (1986 April 5). These distributions are not normalized, so as to simultaneously show the overall decay of the network as well as changes in its size distribution. The distribution farthest in the lower left is that of simulation 1, corresponding to the "true" baseline quiet Sun within our simulation framework. The low end of all distributions, below 10^{19} Mx, are well-fit by a power-law with index −2.12.

The distribution of magnetic flux values remains essentially invariant below $\sim 10^{19}$ Mx, maintaining its power-law shape and logarithmic slope. This is not the case in the flux range 10^{19}—10^{21} Mx, where scale invariance is broken by our size-dependent decay probability. Note however that the very high end of the distribution changes comparatively less over the time span covered here, a consequence of the very largest clusters having a (mean) lifetime in excess of 5 yr. This may be an unrealistic consequence of the size-dependent relationship we assumed for the probability p_s of spontaneous disappearance of clusters (assumed to occur via convective submergence):

$$p_s = (\tau_s \sqrt{n_e})^{-1} \ , \tag{1}$$

where n_e is the number of elementary flux tubes in the cluster, and $\tau = 6.9$ d is the lifetime parameter. This decay model was tuned in Crouch et al. (2007) to reproduce as best as possible the size distribution and spatial distribution of network elements in local "quiet Sun" simulations where the largest clusters barely reached 10^{20} Mx in flux. Extrapolating eq. (1) to clusters with flux $\sim 10^{22}$ Mx thus takes us well beyond the flux range in which it was calibrated. Nonetheless, Figure 13 indicate that the magnetic memory of cycle 21 persists here for many years, even at intermediate flux values reaching into the upper part of the calibration range for eq. (1).

The filling factor recovery time was estimated for the case where the largest polar clusters (those with fluxes exceeding 10^{22} Mx) were omitted. It turns out the recovery time then goes from 2.9 yr to 1.9 yr.

Sunspot cycle 23 had a significantly lower amplitude than cycle 21, as well as a waning phase more extended temporally. Care is thus warranted in directly carrying over our modelling results for cycle 21 to cycle 23. This caveat notwithstanding, taking at face value the network recovery time $\simeq 3$ yr resulting from our cycle 21 modelling would indicate

that the base state of solar photospheric magnetism had *not* yet been reached in the first half of 2009, the deepest portion of the extended cycle 23–24 minimum. Indeed, directly transposing Fig. 12 to cycle 23 would place the return to a true quiet Sun state well into the year 2011, 2010 if large polar clusters are omitted.

6. Conclusion

We have presented in this Paper a simulation of the solar photospheric magnetic network evolving over a full solar cycle. The simulation incorporates statistically uniform magnetic flux injection all over the photosphere, as well as flux injection through the emergence and subsequent decay of active regions. Although formulated as a Monte Carlo simulation reducing the full magnetohydrodynamical complexity of the problem to a simple point-particle interactions and probabilistic rules, the model fares quite well in capturing a number of observed properties of the magnetic network, including its power-law form, fractal index of large network elements, and length scale characterizing the spatial distribution of network elements. The cycle-length simulation also reproduces many observed global properties, including the buildup of a dipole component, in agreement with observations and other modelling approaches to surface magnetic flux evolution. Amongst the quantitative failures of the model, the most prominent is arguably the very high unsigned flux values attained in polar regions in the late phases of the cycle. This results in part from the long lifetimes of the large clusters forming in our simulation, but also from the absence of a global polar sink associated with downward entrainement by the meridional flow.

The simulated distribution of magnetic flux in the polar caps also shows some striking similarities to recent magnetographic observations, notably the fact that most of the flux is concentrated in large, unipolar magnetic concentrations, with the flux of the largest

concentrations carrying the bulk of the signed flux (Shiota et al. 2012). Polar behavior being an integrated result of low-latitude activity and poleward flux transport over solar cycle timescales, the good match with these observations suggests that despite its simplicity, our model succeeds in catching the salient aspects of the underlying physical mechanisms governing the evolution of the magnetic network on these long timescales.

In the late descending phase of our modeled cycle 21, the magnetic flux and filling factor are found to decay exponentially, with an e-folding time of 2.9 yr. We performed a numerical experiment whereby the simulation was extended beyond the last cycle 21 active region emergence, without any cycle 22 active region injection, to follow this exponential decay until the network had recovered its "quiet Sun" distribution used as initial condition to the simulation. In this manner we mimic the onset of a Grand Minimum in activity, and simulate the relaxation of the magnetic network to its baseline state. Applied at face value to the extended activity minimum between cycles 23 and 24, this long decay time indicates that even as late as 2009, the network had not yet reached its baseline state, as it still carried "memory" of active region emergences throughout cycle 23. In the absence of cycle 24 active region emergences, this magnetic network memory would have persisted well into 2011. Even with the removal of the contribution from the largest polar clusters, and its corresponding e-folding time of 1.9 yr, the conclusion that the baseline state had not been reached by late 2009 remains valid. On the other hand, our model also shows that the network is most persistent in polar regions, so that its impact on total and spectral irradiance may have remained modest. This issue clearly deserves further detailed investigation.

We are most grateful to N.R. Sheeley, Jr. and Y.-M. Wang for kindly making their cycle 21 database their database available to us. Thanks also to Nicolas Lawson for

assistance in producing some of the figures, and to an anonymous referee for a constructive report. K.T. is supported in part by a graduate fellowship from FQRNT/Québec. Simulations were made possible by time alocation on the Calcul-Québec/Calcul-Canada computing infrastructures.

REFERENCES

Allen, M. P. & Tildesley, D. J. 1990, Computer Simulation of Liquids, New York: Oxford University Press

Babcock, H.W. 1961, ApJ, 133, 572

Babcock, H.D. 1959, ApJ, 130, 364

Beer, J. 2000, Sp. Sci. Rev., 94, 53

Blanco Rodriguez, J., Okunev, O.V., Puschmann, K.G., Kneer, F., Sanchez-Andrade Nuno, B. 2007, A&A, 474, 251

Charbonneau, P. 2010, Living Reviews in Solar Physics, 7

Cranmer, S.R. & van Ballegooijen, A.A. 2010, ApJ, 720, 824

Crouch, A.D., Charbonneau, P., Thibault, K. 2007, ApJ, 662, 715

de Wijn A.G., Stenflo J.O., Solanki, S.K., Tsuneta S. 2009, Space Sci Rev, 144, 275

Fan, Y. 2009, Living Reviews in Solar Physics, 4

Foukal, P.V., Ortiz, A., & Schnerr, R. 2011, ApJL, 733, L38

Foukal, P.V. 2004, Solar Astrophysics (2nd ed.), New York, Wiley-VCH

Foukal, P.V., Lean, J. 1988, ApJ, 328, 347

Hagenaar, H.J., Schrijver, C.J., & Title, A.M. 2003, ApJ, 584, 1107

Ishikawa, R. & Tsuneta, S. 2009, A&A, 495, 607

Ishikawa, R., Tsuneta, S., Jurcak, J. 2010, ApJ, 713, 1310

Ito, H., Tsuneta, S., Shiota, D., Tokumaru, M., Fujiki, K. 2010, ApJ, 719, 131

Jin, C.L., Wang, J.X. 2012, ApJ, 745, 39

Krijger, J.M. & Roudier, T. 2003, A&A, 403, 715

Leighton, R.B. 1969, ApJ, 156, 1

Martin, S.F. 1988, Sol. Phys., 117, 243

Mattson, W., Rice, B. M. 1999, Computer Physics Communications 119, 135

McIntosh, S.W., Leamon, R.J., Hock, R.A., Rast, M.P., Ulrich, R.K. 2011, ApJ, 730, L3

Meunier, N., Roudier, T., Rieutord, M. 2008, A&A, 488, 1109

Meyer, K.A., Mackay, D.H., van Ballegooijen, A.A., Parnell, C.E. 2011, Sol. Phys., 272, 29

Okunev, O.V. & Kneer, F. 2004, A&A, 425, 321

Orozco Suarez, D., Bellot Rubio, L.R., del Toro Iniesta, J.C., et al. 2007, ApJ, 670, L61

Parnell, C.E. 2001, Sol. Phys., 200, 23

Parnell, C.E., DeForest, C.E., Hagenaar, H.J., Johnston, B.A., Lamb, D.A., Welsch, B.T. 2009, ApJ, 698, 75

Petrovay, K., Van Driel-Gesztelyi, L. 1997, Sol. Phys., 176, 249

Raju, K.P., Srikanth, R., Singh, J. 1998, Sol. Phys., 180, 47

Rast, M.P. 2003, ApJ, 597, 1200

Rieutord, M. & Rincon, F. 2010, Living Reviews in Solar Physics, 2

Rimmele, T., Schroter, E.H. 1989, A&A, 221, 137

Schrijver, C.J., De Rosa, M.L., Title, A.M. 2002, ApJ, 577, 1006

Schrijver, C.J., & Harvey, K.L. 1994, Sol. Phys., 150, 1

Schrijver, C.J., Title, A.M., van Ballegooijen, A.A., Hagenaar, H.J., Shine, R.A. 1997, ApJ, 487, 424

Schrijver, C.J. 2001, ApJ, 547, 475

Schrijver, C.J., Livingston, W.C., Woods, T.N., Mewaldt, R.A. 2011, GRL, 38, L06701

Shiota, D., Tsuneta, S., Shimojo, M., Sako, N., Orozco Suarez, D., Ishikawa, R. 2012, ApJ, 753, 157

Simon, G.W., Title, A.M., Weiss N.O. 2001, ApJ, 561, 427

Srikanth, R., Singh, J., Raju, K.P. 2000, ApJ, 534, 1008

Stenflo, J.O. 2013, A&AR, 21, 66

Tapping, K.F., Boteler, D., Charbonneau, P., Crouch, A., Manson, A., Paquette, H. 2007, Sol. Phys., 246, 309

Tapping, K.F. & Valdes, J.J. 2011, Sol. Phys., 272, 337

Thibault, K., Charbonneau, P., Crouch, A.D. 2012, ApJ, 757, 187

Tsuneta, S., Ichimoto, K., Katsukawa, Y. et al. 2008, ApJ, 688, 1374

Wang, Y.-M., Nash, A. G., Sheeley, N.R. Jr. 1989a, Science, 245, 712

Wang, Y.-M., Nash, A. G., Sheeley, N.R. Jr. 1989b, ApJ, 347, 529

Wang, Y.-M., & Sheeley, N.R. Jr. 1989, Sol. Phys., 124, 81

Wang, Y.-M., & Sheeley, N.R. Jr. 1991, ApJ, 375, 761

Wang, Y.-M., & Sheeley, N.R. Jr. 1994, ApJ, 430, 399

Wang, Y.-M., Sheeley, N.R. Jr., & Lean, J. 2002, ApJ, 580, 1188

Wang, Y.-M., Lean, J., Sheeley, N.R. 2005, ApJ, 625, 522

Wang, J., Wang, H., Tang, F., Lee, J.W., & Zirin, H. 1995, Sol. Phys., 160, 277